argument that the 1T' phase is located in the upper layer (Fig. 1E). Furthermore, no MoO_3, TeO_2, or other elements were observed in the SPEM results [figs. S8 and S9 (19)], which is consistent with the Raman spectroscopy results in Fig. 1. This demonstrates a clean heterophase homojunction structure without oxides or other elements by our phase patterning, which is an advantage compared with the precedent of metastable phase engineering with MoS_2 by a chemical method (7).

The structural transformation process during phase patterning was clarified by in situ scanning transmission electron microscopy (STEM) with a monolayer of 2H-$MoTe_2$ (Fig. 4). Of the two major physical processes, local heating and valence electron excitation related to laser irradiation, we explored the former on the atomic scale. In Fig. 4A, the atomic images obtained at $T = 400°C$, similar to the estimated temperature during laser irradiation, primarily show Te atoms of 2H-$MoTe_2$. Although Te atoms can be sublimated at $T = \sim400°C$ (16), the monolayer 2H phase region remained robust without generating Te vacancies (Fig. 4A). To slightly stimulate the temperature effect, we used a scanning electron beam irradiation (with a beam size of 1 Å and a beam current of 20 pA). Then, low-density atomic Te defects were created (Fig. 4B), and, more important, a clear sign of the structural phase transition from the 2H to 1T' phases was observed in Fig. 4C, which is a fast Fourier-transform (FFT) image of Fig. 4B. Although the hexagonal symmetry remains, as shown by the lattice symmetry of 2H-$MoTe_2$, extra periodic spots with a rectangular symmetry appear in Fig. 4C. The rectangular lattice symmetry is a feature of distorted octahedral (1T') $MoTe_2$ (16, 22).

In contrast to 2H-$MoTe_2$, in which two Te atoms completely overlap in the top view of the crystal in the STEM images, 1T'-$MoTe_2$ should show split Te positions in the top view STEM image (Fig. 1A). The initial stage of splitting the Te atom positions is captured in Fig. 4D, which is a filtered STEM image to clearly show the Te atoms. As marked by two circles and an arrow, the Te atoms start splitting but do not yet completely reach the 1T' phase over the entire area. No such split or rectangular symmetry in FFT was observed without Te vacancies in the monolayer of 2H-$MoTe_2$. This result indicates that the phase transition originates from the Te vacancies at an elevated temperature, either by laser irradiation or by a heating stage. An atomic vacancy is shown in Fig. 4E.

Our density functional theory (DFT) calculations that explain the phase transition by the Te vacancy are shown in Fig. 4F. To select the most stable phase at a low temperature, the relative binding energy per unit formula between the 2H and 1T' phases is plotted as a function of Te vacancy concentration in Fig. 4F. It is clear that a Te monovacancy concentration exceeding 3% causes the 1T' phase to be more stable than the 2H phase, which is qualitatively consistent with our experimental results. Furthermore, the band alignment of ohmic contact at the homojunction of the 2H and the 1T' phases of $MoTe_2$ was veri-

fied by our DFT calculations (19). Compared with the Schottky contact between 2H-$MoTe_2$ and the Au electrode, the interlayer charge transfer across the homojunction in $MoTe_2$ causes only a slight energy difference between the electron affinity of 2H-$MoTe_2$ and the work function of atomically thin 1T'-$MoTe_2$.

The reverse phase transition from the 1T' to the 2H phase was not observed by laser irradiation, even with a higher energy or intensity of the laser. In previous studies (23, 24), temperature has been considered as the primary origin of the phase transition, but the irreversible phase change from the 2H to 1T' phase cannot be explained simply by the thermodynamic reaction in the phase diagram. Moreover, the estimated temperature by laser irradiation ($\sim400°C$) is markedly lower than the reported temperature ($880°C$) for the phase transition. A possible scenario for the one-way phase transition is the strain effect originating from thermal expansion, but the expected thermal coefficient ($\sim10^{-6}$ K^{-1}) produces substantially less lattice strain ($\sim0.05\%$) than the required amount of strain ($\sim5\%$) for the phase transition (15). Thus, the driving force for the phase patterning is the irreversible Te vacancy created by laser irradiation, as verified in the STEM experiment.

REFERENCES AND NOTES

1. Q. H. Wang, K. Kalantar-Zadeh, A. Kis, J. N. Coleman, M. S. Strano, *Nat. Nanotechnol.* **7**, 699–712 (2012).
2. M. Chhowalla et al., *Nat. Chem.* **5**, 263–275 (2013).
3. A. Y. C. Yu, *Solid-State Electron.* **13**, 239–247 (1970).
4. S. Das, H.-Y. Chen, A. V. Penumatcha, J. Appenzeller, *Nano Lett.* **13**, 100–105 (2013).
5. K.-E. Byun et al., *Nano Lett.* **13**, 4001–4005 (2013).
6. W. S. Leong et al., *ACS Nano* **9**, 869–877 (2015).
7. R. Kappera et al., *Nat. Mater.* **13**, 1128–1134 (2014).
8. E. Morosan et al., *Nat. Phys.* **2**, 544–550 (2006).
9. B. Sipos et al., *Nat. Mater.* **7**, 960–965 (2008).
10. J. T. Ye et al., *Science* **338**, 1193–1196 (2012).
11. D. W. Shen et al., *Phys. Rev. Lett.* **99**, 216404 (2007).
12. Y. J. Zhang, T. Oka, R. Suzuki, J. T. Ye, Y. Iwasa, *Science* **344**, 725–728 (2014).
13. G. Eda et al., *ACS Nano* **6**, 7311–7317 (2012).
14. Y.-C. Lin, D. O. Dumcenco, Y.-S. Huang, K. Suenaga, *Nat. Nanotechnol.* **9**, 391–396 (2014).
15. K.-A. N. Duerloo, Y. Li, E. J. Reed, *Nat. Commun.* **5**, 4214 (2014).
16. D. H. Keum et al., *Nat. Phys.* **11**, 482–486 (2015).
17. Y.-F. Lin et al., *Adv. Mater.* **26**, 3263–3269 (2014).
18. N. R. Pradhan et al., *ACS Nano* **8**, 5911–5920 (2014).
19. Supplementary materials are available on *Science* Online.
20. M. Yamamoto et al., *ACS Nano* **8**, 3895–3903 (2014).
21. G. H. Han et al., *ACS Nano* **5**, 263–268 (2011).
22. J. Heising, M. G. Kanatzidis, *J. Am. Chem. Soc.* **121**, 638–643 (1999).
23. M. B. Vellinga, R. de Jonge, C. Haas, *J. Solid State Chem.* **2**, 299–302 (1970).
24. A. Conan, A. Bonnet, A. Amrouche, M. Spiesser, *J. Phys.* **45**, 459–465 (1984).

BIOLOGICAL ADHESIVES

Adaptive synergy between catechol and lysine promotes wet adhesion by surface salt displacement

Greg P. Maier,[1]* Michael V. Rapp,[2]* J. Herbert Waite,[3]† Jacob N. Israelachvili,[2,4]† Alison Butler[1]†

In physiological fluids and seawater, adhesion of synthetic polymers to solid surfaces is severely limited by high salt, pH, and hydration, yet these conditions have not deterred the evolution of effective adhesion by mussels. Mussel foot proteins provide insights about adhesive adaptations: Notably, the abundance and proximity of catecholic Dopa (3,4-dihydroxyphenylalanine) and lysine residues hint at a synergistic interplay in adhesion. Certain siderophores—bacterial iron chelators—consist of paired catechol and lysine functionalities, thereby providing a convenient experimental platform to explore molecular synergies in bioadhesion. These siderophores and synthetic analogs exhibit robust adhesion energies ($E_{ad} \geq -15$ millijoules per square meter) to mica in saline pH 3.5 to 7.5 and resist oxidation. The adjacent catechol-lysine placement provides a "one-two punch," whereby lysine evicts hydrated cations from the mineral surface, allowing catechol binding to underlying oxides.

Water disrupts adhesion on polar surfaces by forming hydration layers that impede intimate contact between adhesive polymers and surfaces. Sessile marine organisms, including barnacles, kelps, and

mussels, routinely adhere to wet saline surfaces, suggesting that successful adaptations for removing weak boundary layers have evolved. Identifying these adaptations holds great promise for adhesion science and technology. The mussel holdfast or

byssus contains ~15 adhesive mussel foot proteins (mfps), two of which, mfp-3 and mfp-5, are deposited first as a primer to condition the target surface and enable other mfps to adhere (1) and are peculiar in containing between 20 and 30 mole percent (mol %) Dopa (3,4-dihydroxyphenylalanine). Demonstration by atomic force microscopy of wet adhesion to titania by a single Dopa (2) sparked functionalization of synthetic polymeric adhesives and self-healing hydrogels with catechol (3–8), but wet adhesion of these polymers to oxides and minerals remains controversial (9, 10). In actuality, mfp-3 and -5 are rich in Lys as well as Dopa, which are frequently in adjacent positions along the protein backbone (1). The surface forces apparatus (SFA) has measured impressive wet adhesion of these proteins to mineral, oxide, and organic surfaces (11). Dopa residues in mfp-3 and -5 form bidentate coordination and hydrogen bonds to mineral and oxide surfaces and hydrophobic interactions on polymeric surfaces (11), but only if protected from oxidation by low pH and antioxidants during deposition (12, 13). Several mimics of mfps have been synthesized, most notably Dopa-Lys copolymers by Yamamoto (14) and Deming (15) using N-carboxyanhydride ring-opening polymerization, as well as the polymer brush anchors

developed by Messersmith (6). However, the role of Lys in both the mussel surface primers and in synthetic wet adhesives remains poorly understood.

Many marine and pathogenic bacteria have evolved an adaptive iron-sequestration pathway that is based on catechol-containing siderophores, including enterobactin, the lactone of tris-2,3-dihydroxybenzoyl-L-Ser (2,3-DHBA-L-Ser) (16). The plant pathogen *Dickeya chrysanthemi* produces the siderophore, cyclic trichrysobactin (CTC), the lactone of tris-2,3-DHBA-D-Lys-L-Ser (Fig. 1A), in which Lys is present adjacent to each catechol (17). The prominence and proximity of catechol and Lys in CTC resemble the interfacial adhesive proteins mfp-3 and mfp-5. However, the mass of CTC (1053 g/mol) is a fraction of the mfp-3 and -5 masses (6 kD and 10 kD, respectively). As such, the siderophore has relaxed steric constraints when adsorbed to a surface, and the simpler siderophore structure allows for more straightforward interpretation of the adhesive mechanisms. In addition, the autoxidation of 2,3-DHBA is much slower than 4-methylcatechol, a proxy for the 3,4-dihydroxy substituents in the Dopa catechol, at pH 7.5 and 10 (fig. S1 and supplementary text), reflecting intramolecular H-bonding between the ortho-OH and the carbonyl oxygen and the electron-withdrawing nature of the carboxylate substituent (Fig. 1B), both of which stabilize CTC against oxidation compared with Dopa in mfps. Ultimately, subtle molecular differences in 2,3-DHBA contribute to the oxidation resistance in siderophores and enlarge the pH range over which these compounds bind to target surfaces.

A SFA was used to measure the normalized force (F/R)–distance (D) profiles of two molecularly

smooth mica surfaces (of radius R) during their approach and separation in buffered solutions of CTC (18). In these SFA measurements, the surfaces are first slowly brought into contact and compressed. The thickness of the intervening compressed film between the surfaces is measured as D_T. The surfaces are then slowly separated, and the adhesion force (F_{ad}/R) is measured at the force minimum, at a point just before the surfaces rapidly jump apart.

Mica is an anionic and molecularly smooth aluminosilicate mineral that allows for Å-level mechanistic insight during adhesion measurements. In saline solutions, mica adsorbs cations (particularly K^+) to form a tightly bound hydration layer at the solid-liquid interface (19, 20). These hydration layers, present at virtually all marine and physiological interfaces, impose a substantial molecular barrier to coatings and high-performance adhesives for wet surfaces (21). The effects of these hydration layers between mica surfaces in buffered solution without any added siderophores (Fig. 1C, black circles) are seen in the SFA measurements: When compressed to 10 mN m^{-1}, hydrated K^+ ions form a $D_T = 13 \pm 1$ Å–thick layer between the mica surfaces, and only a weak adhesion force is measured on separation. However, nanomole amounts of CTC form a single monolayer "molecular bridge" that results in a large adhesion force between the micas, presumably by displacing the hydrated salt ions from the mica surface (Fig. 1C, red circles). After injecting 10 nanomoles of CTC into the buffered gap solution between the mica surfaces (~50 μL total volume, 200 μM bulk concentration), the compressed film thins to 11 ± 1 Å, indicating that the hydrated salt ions have been

¹Department of Chemistry and Biochemistry, University of California, Santa Barbara, CA 93106, USA. ²Department of Chemical Engineering, University of California, Santa Barbara, CA 93106, USA. ³Molecular, Cellular, and Developmental Biology, University of California, Santa Barbara, CA 93106, USA. ⁴Materials Department, University of California, Santa Barbara, CA 93106, USA.
*These authors contributed equally to this work.
†Corresponding author. E-mail: herbert.waite@lifesci.ucsb.edu (J.H.W.); jacob@engineering.ucsb.edu (J.N.I.); butler@chem.ucsb.edu (A.B.)
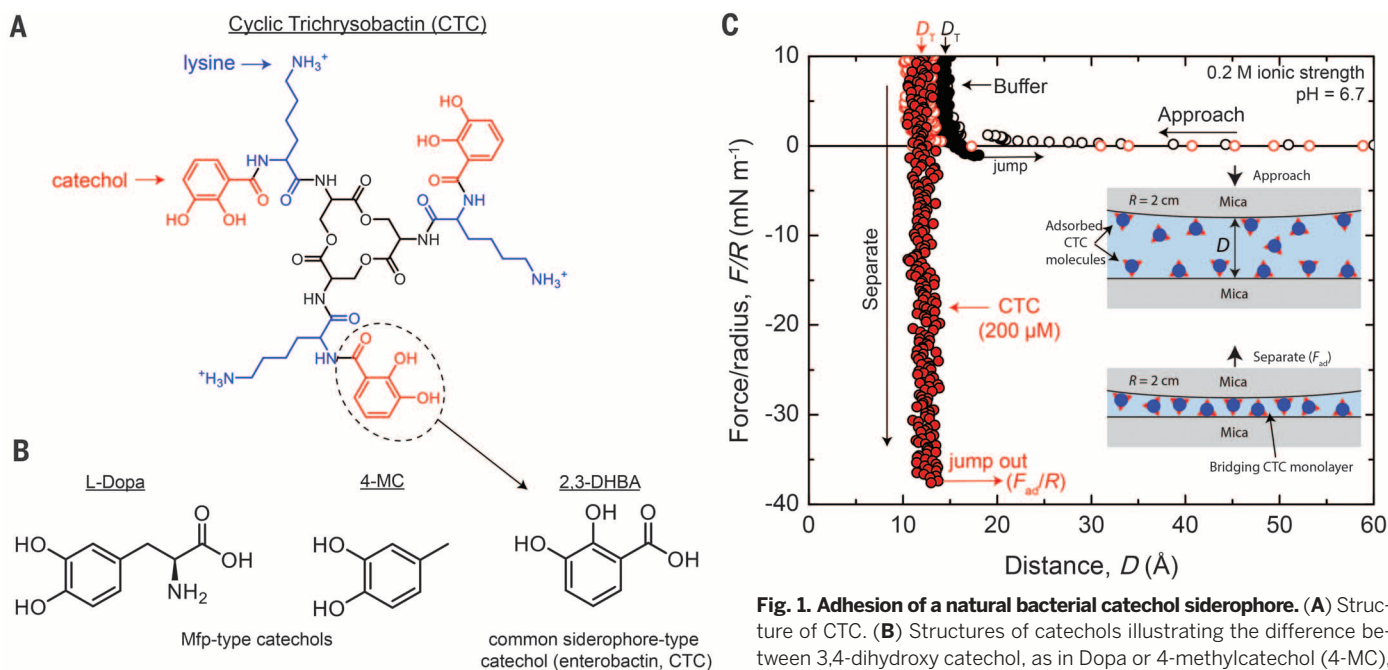
Fig. 1. Adhesion of a natural bacterial catechol siderophore. (A) Structure of CTC. (B) Structures of catechols illustrating the difference between 3,4-dihydroxy catechol, as in Dopa or 4-methylcatechol (4-MC), and 2,3-dihydroxy catechol, as commonly present in DHBA-containing siderophores. (C) SFA force-distance interaction for CTC-mediated adhesion between two mica surfaces in buffer (50 mM phosphate buffer + 150 mM KNO₃) at pH 6.7. The surfaces were left in contact for 30 min before separation. The open and solid circles are for data measured on approach and separation, respectively, of the mica surfaces. The inset displays a schematic of the interacting surfaces throughout the SFA experiments.

A Tren-Lys-Cam (TLC)

B

C

Fig. 2. Adhesion of a synthetic siderophore mimic. (**A**) Structure of TLC, a synthetic mimic of the natural siderophore CTC. (**B**) SFA force-distance interaction for the TLC-mediated adhesion between two mica surfaces in buffer (50 mM acetate buffer + 150 mM KNO$_3$) at pH 3.3. The surfaces were left in contact for 30 min before separation. The open and solid circles are for data measured on approach and separation, respectively, of the mica surfaces. The inset displays a schematic of the interacting surfac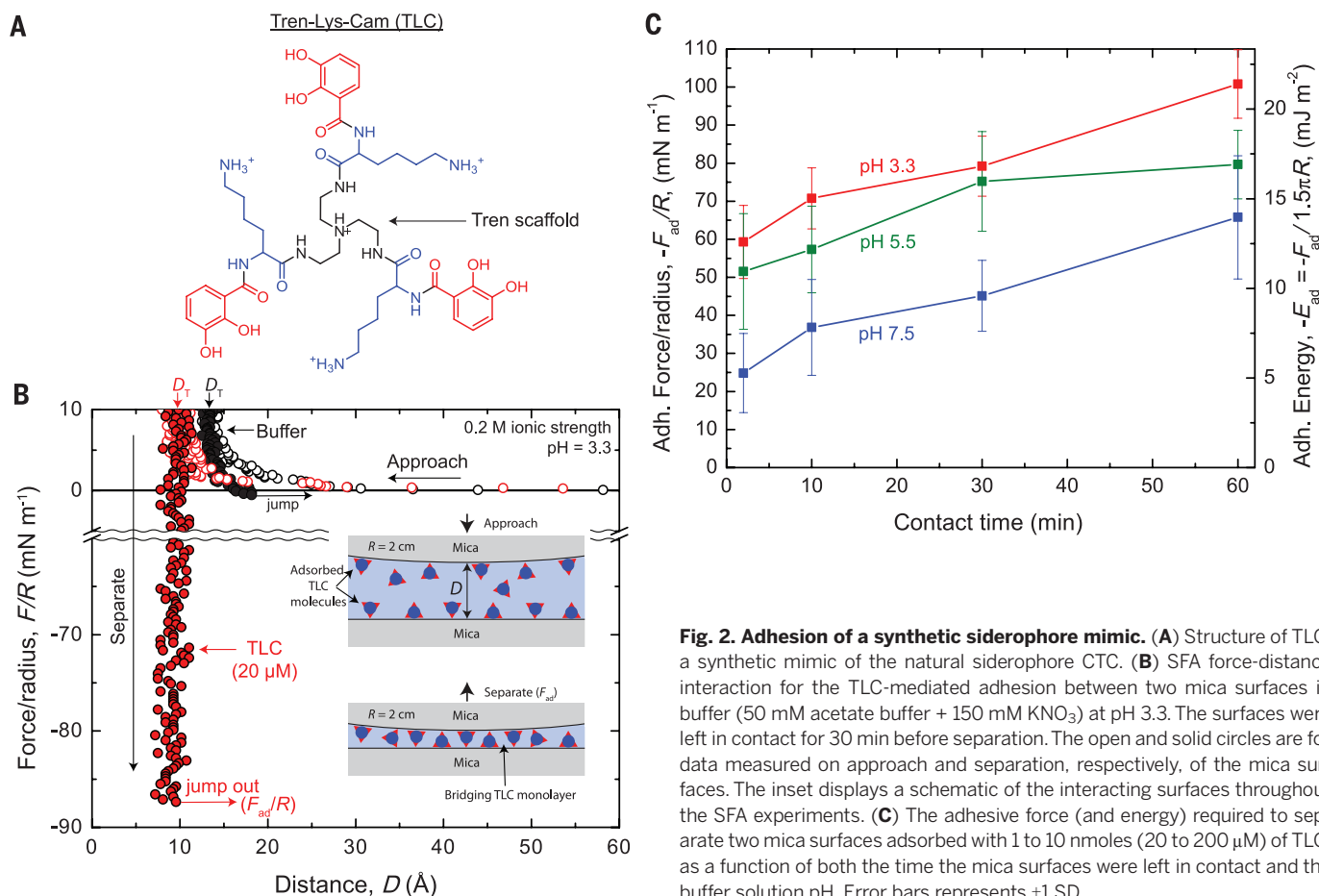es throughout the SFA experiments. (**C**) The adhesive force (and energy) required to separate two mica surfaces adsorbed with 1 to 10 nmoles (20 to 200 μM) of TLC, as a function of both the time the mica surfaces were left in contact and the buffer solution pH. Error bars represents ±1 SD.

replaced with CTC at the surface, and the adhesion force between the surfaces increases by a factor of approximately 30-fold to ~30 ± 10 mN m^{-1}. As the surfaces are separated, the sharply vertical shape of the separation force curve does not exhibit any observable bridging (i.e., an increase in the separation distance), indicating that the physical bonds supporting adhesion are specific and short-ranged (effective only over several Å), such as a hydrogen bond or specific Coulombic interaction (20).

The natural 2,3-DHBA–containing CTC siderophore promotes adhesion at near-neutral pH (pH 6.7), a solution condition that rapidly oxidizes Dopa in mfps leading to reduced adhesion (12). Yet, the triserine lactone scaffold of CTC hydrolyses under acidic conditions, limiting its usefulness as an adhesive primer over a wide range of pH. To circumvent this limitation, we synthesized a mimic of CTC, Tren-Lys-Cam (TLC) (Fig. 2A) built on the robust tris(2-aminoethyl)amine (Tren) scaffold that retains integrity over a wide pH range (fig. S2) (22). TLC exhibits nearly identical adsorption and adhesion behavior to the natural CTC siderophore. In parallel SFA experiments at pH 3.3 (Fig. 2B), TLC molecules displace hydrated salt ions at the mica surface and, after compression of the surfaces, form a 9 ± 1 Å–thick monolayer that bridges between the two surfaces. The thickness of the TLC film, the shape of the force-distance

profile (narrow adhesion well), and dramatically increased adhesion all indicate that the synthetic TLC performs similarly to CTC at mineral surfaces.

TLC mediates adhesion between mineral surfaces in saline solution from pH 3.3 to 7.5 (Fig. 2C). The TLC peak adhesion concentration is ~20 μM (fig. S3). Adhesion forces measured in SFA experiments are converted to adhesion energies through the Johnson-Kendal-Roberts theory of adhesive surfaces ($E_{ad} = F_{ad}/1.5\pi R$) (23). Adhesion is strongest at pH 3.3 and is not statistically different from pH 5.5 for $P \leq 0.05$ (table S1). At pH 7.5, adhesion decreases ($P \leq 0.05$), yet TLC still maintains ~65% of the peak adhesion. The cause for the decrease in adhesion at pH 7.5 is under investigation; we speculate that either slow TLC oxidation or subtle interfacial pH changes reduce the number of bridging hydrogen bonds at pH 7.5. Moreover, adhesion energy increases with contact time before separation, a common trait among adhesives. As longer contact allows for better interfacial equilibration, more siderophore molecules are able to rearrange and maximize the number of bridging bonds (20).

To ascertain specific contributions made by catechol and Lys in the siderophore adhesive platform, we synthesized a suite of five additional Tren-based homologs, varying properties of the amine and the aromatic functionalities (Fig. 3, A to G; figs. S4 to S13; and tables S2 to S4). Group I homologs retain both catechol and amine functionalities (Fig. 3, B

and C), group II retains Lys but removes the catechol functionality (Figs. 3D and 3E), and group III retains catechol but removes the amine functionality (Figs. 3F and 3G). Collectively, the results of the six synthetic homologs reveal a requirement for catechol and an alkylamine cation (e.g., Lys and Dab) for appreciable surface binding and adhesion.

Group I includes TLC and Tren-Dab-Cam (TDC), with the Lys chain shortened by two methylene units to diaminobutyric acid (Dab). Group I assesses whether the length or flexibility of the amine is critical to adsorption and adhesion. The length of the amine chain between 2 and 4 carbons does not alter the homolog's behavior, because both TLC and TDC displace salt on the mica surface and promote large adhesion energies (Fig. 3, H and I, and fig. S14C).

Group II homologs test the effect of removing catechol, while maintaining the 4+ cationic charge: Tren-Lys-Pam (TLC) retains one hydroxyl group, whereas Tren-Lys-Bam (TLB) removes both hydroxyls. Without catechol, the group II homologs exhibit comparatively weak adhesion between mica surfaces—i.e., ~15% of the group I homologs with both Lys and catechol. Contrary to the narrow adhesion wells of the group I homologs, the separation force curves of group II homologs display weak bridging (~5 to 10 Å) before the surfaces jump apart (fig. S14, A and B), suggesting that the adhesion may be due to nonspecific interactions
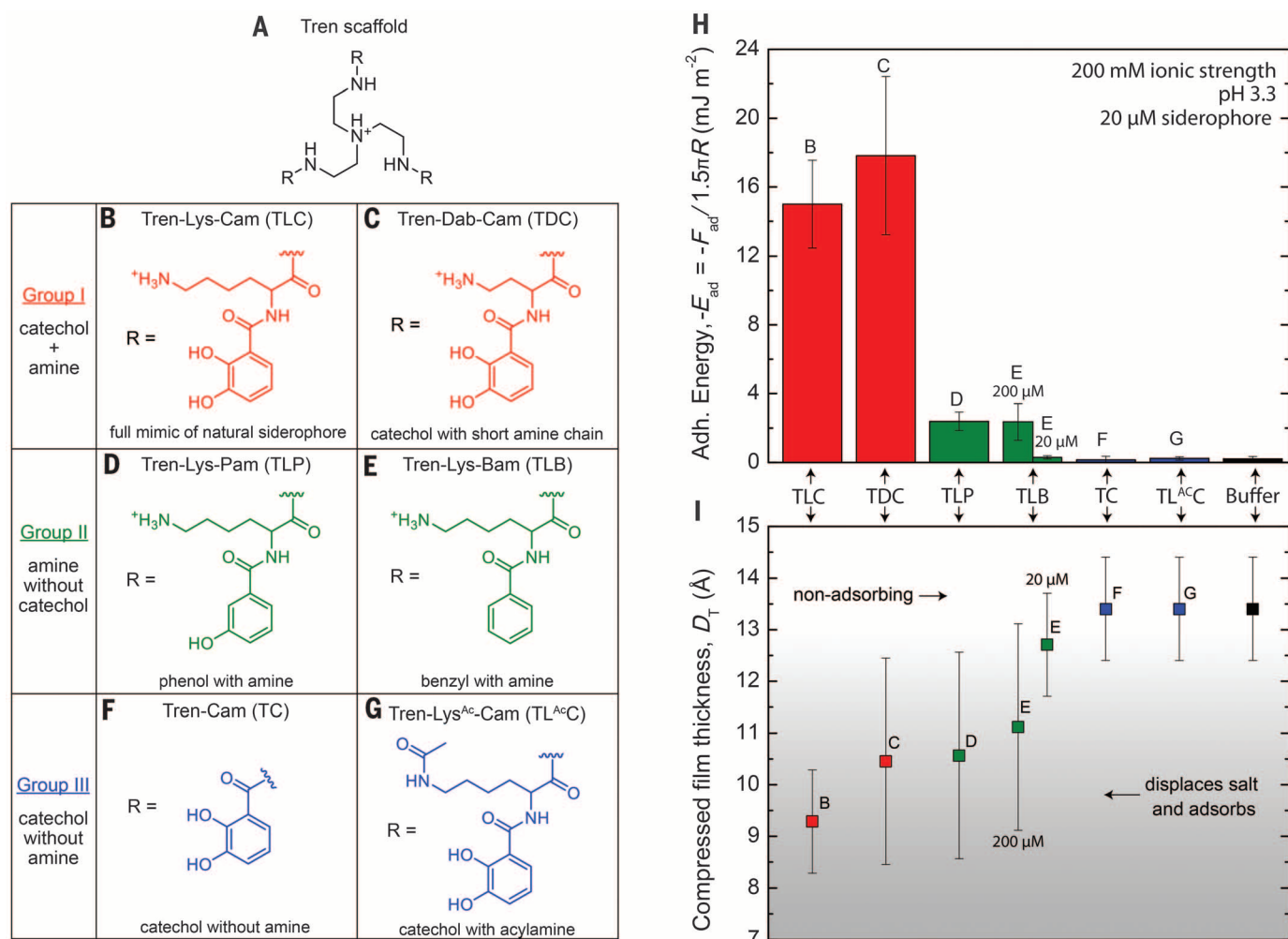
Fig. 3. The synergy of catechol and Lys in siderophore adhesion. (**A**) Structure of the Tren scaffold. (**B** to **G**) The R groups appended to Tren. (**H**) The average adhesion energy required to separate two mica surfaces adsorbed with 1 nmole (20 µM, except where indicated at 200 µM) of the homolog in buffer (50 mM acetate + 150 mM KNO$_3$) at pH 3.3 after 10 min of contact. (**I**) D_T of the siderophore monolayer between two mica surfaces at 10 mN/m of compressive load. The film thicknesses correspond with the adhesion energy displayed in (H). A decreased film thickness (<12 Å) indicates that homologs B, C, D, and E (200 µM) adsorb, displace hydrated salt at the mica surface, and mediate adhesion between two mica surfaces. SFA force-distance measurements for each molecule are shown in figs. S14 and S15.

between two or more homologs (such as hydrophobic interactions or π-cation interactions) (*24*). TLB is unable to donate H bonds and has increased hydrophobicity; hence, it has an increased energy barrier for adsorption. TLP adsorbs to the mica surface at 20 µM (the same as the TLC critical aggregation concentration), yet TLB requires an elevated bulk concentration of 200 µM before adsorption begins.

Group III homologs compromise the amine functionality through acetylation [Tren-Lys^{Ac}-Cam (TL^{Ac}C)] or by omission of Lys [Tren-Cam (TC)], while maintaining the catechol presence. Over the concentration range of 2 to 200 µM, group III homologs do not adsorb on the mica surface at high salt (µ = 200 mM) and provide no adhesion (fig. S15, A and B). In pure water, TC adsorbs as a multilayer on mica and demonstrates modest cohesion (fig. S15C).

In sum, the amine and catechol moieties interact synergistically to mediate surface priming by the catechol alkylamine compounds to mineral surfaces.

Bidentate catechol-mediated H-bonding is necessary for robust bridging attachments between surfaces; however, catechols alone are insufficient to breach the hydrated salt layer on mica, which is typical of a wide variety of aluminosilicate minerals in its cation binding properties (*25*). The amines in CTC and TLC may serve as molecular vanguards to displace hydrated salt ions and ready the surface for bidentate catechol binding (*26*).

The discovery that 2,3-dihydroxycatechol and alkyl ammonium (e.g., Lys and Dab) functionalities limit oxidation and promote adhesion has relevance to other adhesive platforms in providing a compelling rationale for the >20 mol % of cationic residues in Dopa-rich mfps (*1*) and establishing a set of design parameters for future bio-inspired synthetic polymers. Because many synthetic adhesives are functionalized with catechols and amines (*27*) for improved solubility (*10*) or cross-linking effects (*28*, *29*), our results highlight the need to couple catechol and cationic functionalities to displace surface salts.

REFERENCES AND NOTES

1. B. P. Lee, P. B. Messersmith, J. N. Israelachvili, J. H. Waite, *Annu. Rev. Mater. Res.* **41**, 99–132 (2011).
2. H. Lee, N. F. Scherer, P. B. Messersmith, *Proc. Natl. Acad. Sci. U.S.A.* **103**, 12999–13003 (2006).
3. M. Krogsgaard, M. A. Behrens, J. S. Pedersen, H. Birkedal, *Biomacromolecules* **14**, 297–301 (2013).
4. H. Shao, R. J. Stewart, *Adv. Mater.* **22**, 729–733 (2010).
5. C. J. Kastrup *et al.*, *Proc. Natl. Acad. Sci. U.S.A.* **109**, 21444–21449 (2012).
6. A. R. Statz, R. J. Meagher, A. E. Barron, P. B. Messersmith, *J. Am. Chem. Soc.* **127**, 7972–7973 (2005).
7. J. Ryu, S. H. Ku, H. Lee, C. B. Park, *Adv. Funct. Mater.* **20**, 2132–2139 (2010).
8. J. D. White, J. J. Wilker, *Macromolecules* **44**, 5085–5088 (2011).
9. Y. Li, M. Qin, Y. Li, Y. Cao, W. Wang, *Langmuir* **30**, 4358–4366 (2014).
10. J. Wang *et al.*, *Adv. Mater.* **20**, 3872–3876 (2008).
11. J. Yu *et al.*, *Proc. Natl. Acad. Sci. U.S.A.* **110**, 15680–15685 (2013).
12. J. Yu *et al.*, *Nat. Chem. Biol.* **7**, 588–590 (2011).
13. N. R. Martinez Rodriguez, S. Das, Y. Kaufman, J. N. Israelachvili, J. H. Waite, *Biofouling* **31**, 221–227 (2015).
14. H. Yamamoto, *J. Chem. Soc., Perkin Trans. 1* 613–618 (1987).
15. M. Yu, J. Hwang, T. Deming, *J. Am. Chem. Soc.* **121**, 5825–5826 (1999).

16. K. N. Raymond, E. A. Dertz, S. S. Kim, *Proc. Natl. Acad. Sci. U.S.A.* **100**, 3584–3588 (2003).
17. M. Sandy, A. Butler, *J. Nat. Prod.* **74**, 1207–1212 (2011).
18. J. Israelachvili *et al.*, *Rep. Prog. Phys.* **73**, 036601 (2010).
19. R. M. Pashley, *Adv. Colloid Interface Sci.* **16**, 57–62 (1982).
20. J. N. Israelachvili, *Intermolecular and Surface Forces: Revised Third Edition* (Academic Press, 2011).
21. J. Israelachvili, H. Wennerström, *Nature* **379**, 219–225 (1996).
22. S. J. Rodgers, C. W. Lee, C. Y. Ng, K. N. Raymond, *Inorg. Chem.* **26**, 1622–1625 (1987).
23. K. L. Johnson, K. Kendall, A. D. Roberts, *Proc. R. Soc. A Math. Phys. Eng. Sci.* **324**, 301–313 (1971).
24. S. Kim *et al.*, *J. Mater. Chem. B* **3**, 738–743 (2015).
25. W. Stumm, J. J. Morgan, *Aquatic Chemistry: Chemical Equilibria and Rates in Natural Waters, 3rd Edition* (Wiley, New York, 1996).
26. Y. Akdogan *et al.*, *Angew. Chem.* **53**, 11253–11256 (2014).
27. P. Podsiadlo, Z. Liu, D. Paterson, P. B. Messersmith, N. A. Kotov, *Adv. Mater.* **19**, 949–955 (2007).
28. F. Zhang, S. Liu, Y. Zhang, Y. Wei, J. Xu, *RSC Adv.* **2**, 8919–8921 (2012).
29. Q. Wei *et al.*, *Angew. Chem. Int. Ed. Engl.* **53**, 11650–11655 (2014).

CHARGE TRANSFER

Efficient hot-electron transfer by a plasmon-induced interfacial charge-transfer transition

K. Wu,[1] J. Chen,[1] J. R. McBride,[2] T. Lian[1]*

Plasmon-induced hot-electron transfer from metal nanostructures is a potential new paradigm for solar energy conversion; however, the reported efficiencies of devices based on this concept are often low because of the loss of hot electrons via ultrafast electron-electron scattering. We propose a pathway, called the plasmon-induced interfacial charge-transfer transition (PICTT), that enables the decay of a plasmon by directly exciting an electron from the metal to a strongly coupled acceptor. We demonstrated this concept in cadmium selenide nanorods with gold tips, in which the gold plasmon was strongly damped by cadmium selenide through interfacial electron transfer. The quantum efficiency of the PICTT process was high (>24%), independent of excitation photon energy over a ~1–electron volt range, and dependent on the excitation polarization.

The surface plasmon resonance (SPR) of metallic nanostructures has been widely used to improve the efficiency of photovoltaics (*1–5*), photocatalysis (*6, 7*), and photodetectors (*8, 9*), either by increasing light absorption through enhanced local fields near the metal nanostructures (*10*) or by plasmon-induced charge transfer from the excited metal (*11–13*). The latter enhancement mechanism suggests the possibility of using plasmonic metal nanostructures as light absorbers with broad spectral tunability, large absorption cross sections, superior long-term stability, and low-cost colloidal synthesis (*14, 15*). Thus far, all reported plasmon-induced charge-separation processes have been believed to occur through a conventional plasmon-induced hot electron transfer (PHET) mechanism (Fig. 1A). During PHET, a plasmon decays into a hot electron–hole pair within the metal via Landau damping on time scales of a few to tens of femtoseconds (*16–18*); this is followed by the transfer of the hot electron into adjacent semiconductors or molecules. Hot-electron transfer competes with electron relaxation through rapid electron-electron scattering in the metal's conduction band (CB) on time scales of hundreds of femtoseconds (*18–20*). Efficient PHET requires interfacial charge separation on an even faster time scale, which is difficult to realize in many semiconductor-metal hybrid materials. Thus, the reported efficiencies for devices based on plasmon-induced charge-separation concepts are too low for practical applications (*6–8*).

Metal-to-semiconductor hot-electron transfer efficiencies can be enhanced if the competition with ultrafast electron-electron scattering in the metal can be avoided. One approach is to create a direct metal-to-semiconductor interfacial charge-transfer transition (DICTT) that can be directly excited to promote an electron from the metal into the semiconductor CB (Fig. 1B). Such transitions between metal adatoms and semiconductor electrodes have been reported (*21*), as have metal-to-adsorbate resonances for CO adsorbed on Pt nanoparticles (NPs) (*22, 23*) and Cs atoms adsorbed on Cu(111) (*24, 25*). However, these interfacial transitions are often too weak as compared with bulk metal transitions or plasmon bands (*22–25*) and cannot serve as efficient light-harvesting pathways. Ideally, a desirable photoinduced hot-electron transfer pathway would combine the strong light-absorbing power of plasmonic transitions with the superior charge-separation properties of the DICTT mechanism (Fig. 1C). In this plasmon-induced metal-to-semiconductor interfacial charge-transfer transition (PICTT) pathway, the metal plasmon serves as a light absorber, but strong interdomain coupling and mixing of the metal and semiconductor levels lead to a new plasmon
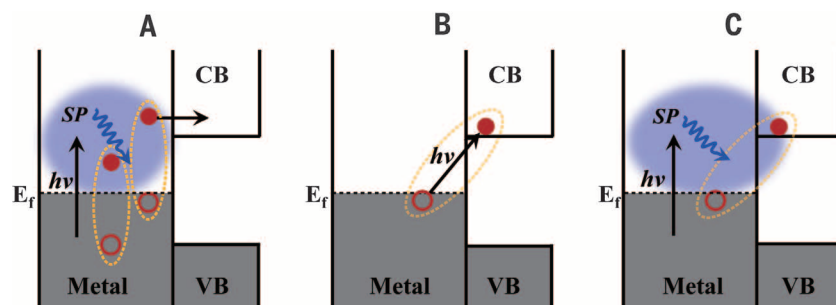

Fig. 1. Metal-to-semiconductor charge-separation pathways. (**A**) Conventional PHET mechanism, in which a photoexcited plasmon (SP, blue ellipsoid) in the metal decays into a hot electron–hole pair (solid and open red circles in the dotted ellipsoids) through Landau damping, followed by injection of the hot electron into the CB of the semiconductor. The electron-hole pair has a broad distribution of initial electron and hole energies; only two are shown for clarity. (**B**) Optical excitation of an electron in the metal directly into the CB of the semiconductor through the DICTT pathway. (**C**) The newly demonstrated PICTT pathway, where the plasmon decays by directly creating an electron in the CB of the semiconductor and a hole in the metal. VB is the semiconductor valence band and *hv* indicates the excitation photons.

[1]Department of Chemistry, Emory University, 1515 Dickey Drive, Atlanta, GA 30322, USA. [2]Department of Chemistry, The Vanderbilt Institute of Nanoscale Science and Engineering, Vanderbilt University, Nashville, TN 37235, USA.
*Corresponding author. E-mail: tlian@emory.edu (T.L.)

Science

Adaptive synergy between catechol and lysine promotes wet adhesion by surface salt displacement

Greg P. Maier, Michael V. Rapp, J. Herbert Waite, Jacob N. Israelachvili and Alison Butler

Keeping it sticky when wet

Some biological molecules are remarkably sticky, even to surfaces submerged in water. Mussel adhesion, for example, is based on the overproduction of dihydroxyphenylalanine (DOPA) and proteins with a high abundance of cationic amine residues such as lysine. Using bacterial iron chelators consisting of paired DOPA and lysine groups as analogs for the mussel proteins, Maier *et al.* show that these two functional groups synergistically enhance interfacial adhesion (see the Perspective by Wilker). The lysine appears to displace hydrated cations from the surface, thus giving a dry patch for better adhesion.

Science, this issue p. 628; see also p. 582

ARTICLE TOOLS	http://science.sciencemag.org/content/349/6248/628
SUPPLEMENTARY MATERIALS	http://science.sciencemag.org/content/suppl/2015/08/05/349.6248.628.DC1
RELATED CONTENT	http://science.sciencemag.org/content/sci/349/6248/582.full
REFERENCES	This article cites 27 articles, 4 of which you can access for free http://science.sciencemag.org/content/349/6248/628#BIBL
PERMISSIONS	http://www.sciencemag.org/help/reprints-and-permissions

Use of this article is subject to the Terms of Service